



## Article

# UAV, GNSS, and InSAR Data Analyses for Landslide Monitoring in a Mountainous Village in Western Greece

Konstantinos G. Nikolakopoulos <sup>\*</sup>, Aggeliki Kyriou , Ioannis K. Koukouvelas , Nikolaos Tomaras and Epameinondas Lyros

Department of Geology, University of Patras, 26504 Patras, Greece; a.kyriou@upnet.gr (A.K.); iannis@upatras.gr (I.K.K.); up1065284@upnet.gr (N.T.); lyrosepameinondas@googlemail.com (E.L.)

\* Correspondence: knikolakop@upatras.gr

**Abstract:** Areas in Western Greece are particularly prone to landslides. Usually triggered by earthquakes or intense rainfalls, they cause damage to infrastructure (roads, bridges, etc.) and human properties. Hence, there is an urgent need for the implementation of monitoring and landslide prevention methodologies. In the last years, Unmanned Aerial Vehicles (UAVs), Global Navigation Satellite Systems (GNSS), and Interferometric SAR (InSAR) techniques have been applied for landslide mapping and monitoring. The current study focuses on the systematic and long-term analysis of a landslide that occurred in Ano Kerasovo village, within the region of Western Greece. To precisely measure the current evolution of the landslide, we performed repetitive UAV campaigns in conjunction with corresponding GNSS surveys, covering a time period between February 2021 and April 2023. The identification of surface modification was based on a change detection approach between the generated point clouds. The results are validated through GNSS measurements and field observations. Added to this, we collected archived Persistent Scatterer Interferometry (PSI) measurements derived from the European Ground Motion Service (EGMS) to extend the observation period and gain a more complete understanding of the phenomenon. It is proven that archived PSI measurements can be used as an indicator of possible landslide initialization points and for small-scale large coverage investigations, while UAVs and GNSS data can precisely identify the microscale deformations (centimeter scale).

**Keywords:** landslides; monitoring; UAV; GNSS; PSI; analysis



**Citation:** Nikolakopoulos, K.G.; Kyriou, A.; Koukouvelas, I.K.; Tomaras, N.; Lyros, E. UAV, GNSS, and InSAR Data Analyses for Landslide Monitoring in a Mountainous Village in Western Greece. *Remote Sens.* **2023**, *15*, 2870. <https://doi.org/10.3390/rs15112870>

Academic Editor: Alex Hay-Man Ng

Received: 30 April 2023

Revised: 26 May 2023

Accepted: 30 May 2023

Published: 31 May 2023



**Copyright:** © 2023 by the authors. Licensee MDPI, Basel, Switzerland. This article is an open access article distributed under the terms and conditions of the Creative Commons Attribution (CC BY) license (<https://creativecommons.org/licenses/by/4.0/>).

## 1. Introduction

Landslides are one of the most common hazards worldwide. Triggered by several factors such as earthquakes, weather extremes, volcanic eruptions, etc., they usually manifest instantly. Apart from modifying Earth's surface, they can cause economic losses and even fatalities [1–4]. Hence, the development of strategies for landslide prevention and mitigation is an essential issue [5,6]. Over the last few years, several studies have been carried out on the utilization of remote sensing data and Geographic Information Systems (GIS) in the investigation of instability phenomena [7,8]. Some of those are analyzing the triggering factors, while others are focusing on the incessant monitoring of landslide-prone locations [9–12].

In particular, Synthetic Aperture Radar Interferometry (InSAR) constitutes one of the most widely known approaches for evaluating topographic changes [13]. Thus, the utilization of InSAR methods to detect and monitor landslides has been well-documented in several studies over the last few years [14–17]. The main advantages of this approach over conventional ones for landslide investigation include the extended spatial coverage, the enhanced spatio-temporal resolution, and the capability of being operated independently of weather conditions. In light of this, advanced InSAR methodologies, based on the multitemporal analysis of SAR data stacks, were applied in order to detect extremely slow

movements estimated at a few mm/year. Persistent Scatterer Interferometry (PSI) and the Small Baseline Subset (SBAS) constitute the most widely used approaches for the long-term monitoring of slow-moving landslides [18–22]. It has been proven that PSI appears to be slightly more accurate compared to the SBAS approach [23]. In more detail, some researchers have utilized PSI measurements derived from the Sentinel-1 constellation to evaluate landslide kinematics and subsequently understand the sliding mechanisms [24], while others focused on creating methodologies for the continuous assessment or update of landslide inventories through PSI measurements [25,26]. Moreover, a post-processing PSI procedure has been proposed for the identification of slowly moving regions in the French Alps and the subsequent extraction of areas of active deformation with velocities lower than 1.6 cm/y [27].

Another well-known solution for landslide monitoring is based on the use of Global Navigation Satellite System (GNSS) sensors [28,29]. Although GNSS measurements for topographic monitoring purposes have been used since the 1990s, the advances in technology and computer science prove that it is still an active field of research. Specifically, different GNSS-based algorithms were developed in order to precisely detect displacements [30], while the adaptive sliding window method was proposed to provide reliable and operational landslide information [31]. Furthermore, low-cost GNSS receivers have been manufactured to evaluate surface deformation in real-time [32,33].

The rise of UAVs has revolutionized landslide investigation due to their survey flexibility, cost efficiency, and high spatial resolution [34,35]. In this framework, numerous studies have been conducted to monitor landslide behavior. [36–41]. The more simplified approaches used Digital Elevation Models (DEMs) extracted by UAV surveys to map and quantify surface changes over landslide areas [42,43] or to monitor waste piles in coal mines [44]. Another successful way to identify topographic modification or any potential displacement relies on the comparison of multitemporal UAV point clouds [45]. Some researchers focused on the assessment of the evolution and dynamics of landslides through the post-processing of UAV products (orthophotos, DEMs, point clouds) [46,47], while others tried to create guidelines for the proper performance of UAV flights for landslide investigations [48–50]. UAV data along with a non-parametric random forest model have also been utilized in order to create landslide susceptibility maps [51]. At the same time, different approaches have been developed for the extraction of 3D displacements via UAV photogrammetry [52,53]. The more sophisticated methodologies deal with the creation of semi-automated or automated models for the rapid recognition of landslides or landslide cracks [54,55].

More multidiscipline studies suggest the combined use of various remote sensing data to monitor ground deformation. In particular, InSAR time series measurements in conjunction with UAV imagery were utilized to analyze the long-term behavior of landslides and improve the understanding of landslide kinematics [56,57]. Moreover, UAVs and GNSS surveys were performed for the validation of SAR methodologies in other case studies [58,59]. Finally, more complex approaches consisted of topo-geodetic and UAV surveys along with ground-penetrating radar and geotechnical data [60].

The current research focuses on the systematic and long-term analysis of instability phenomena in a mountainous area of Western Greece. To precisely monitor the recent evolution of the landslide, we performed repetitive UAV campaigns in conjunction with corresponding GNSS surveys. The identification of surface deformation was based on a change detection approach between the generated point clouds. The results were validated through GNSS measurements and field observation. Added to this, we collected archived PSI measurements derived from the European Ground Motion Service (EGMS) to extend the observation period and gain a more complete understanding of the phenomenon. With regard to this, the novelty of the current research relies on the exploitation of archived PSI measurements as potential future landslide indicators. In addition to the aforementioned points, the synergistic use of various remote sensing data provides the necessary information to study instability at different scales. Specifically, PSI measure-

ments are ideal for monitoring large areas, while UAV and GNSS surveys are suitable for monitoring smaller areas.

## 2. Study Area

### 2.1. Location and Geological Setting

The landslide area is located on the outskirts of Ano Kerasovo village within the region of Western Greece (Figure 1). The area belongs to the Ionian geotectonic unit, which dominates most of the Epirus and Akarnania regions, parts of the Ionian Islands, and continues southwards to the Peloponnese, Crete, and Dodecanese Islands. It consists primarily of Mesozoic carbonates and minor cherts and shales. Oligocene flysch has overlain the Mesozoic carbonates. Flysch is composed of different rhythmic alternations of competent/strong sandstone layers with low-strength siltstone/clayey schist beds. The specific formation is generally associated with intensive folding and fracturing. During the upper Eocene to lower Miocene, the area participated in the Alpine orogenic belt during a Tertiary age collision with westward propagating intracontinental thrusting [61–64].

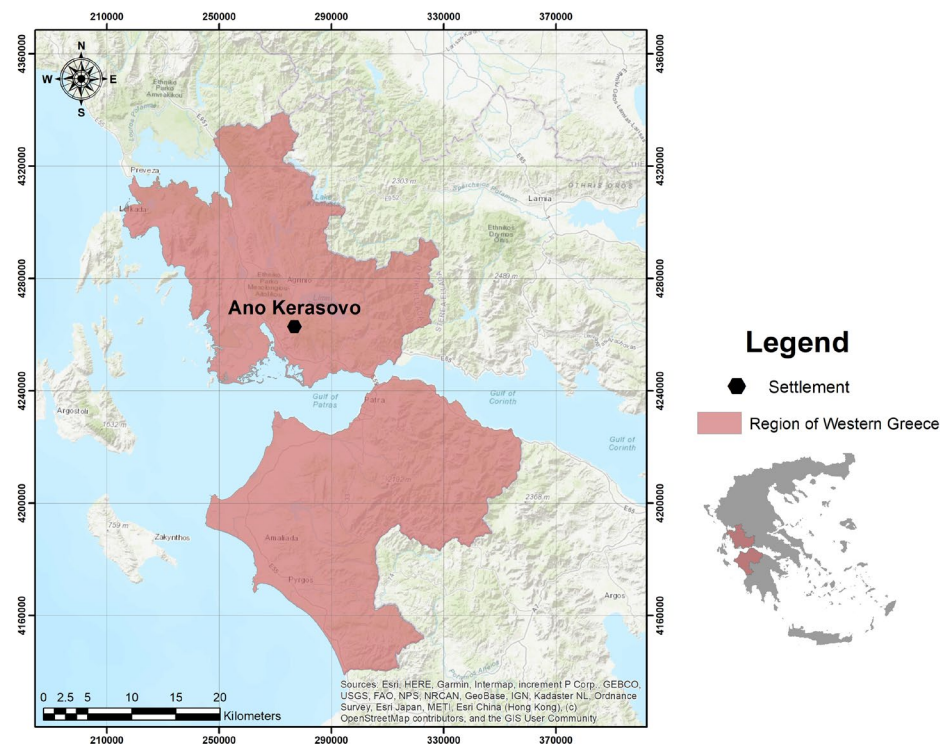


**Figure 1.** Location of the area of interest.

Geomorphologically, the area of interest is characterized by successive ridges and gullies oriented across a southeast facing bluff that flanks the Platanius River. Ringes' prevailing lithology is the Oligocene Arakynthos sandstones [65], while gullies consist of sand and clay alternations. A weathering zone ranging from 0.5 to 7 m thick is being developed in these gullies. This zone is characterized by chaotic material accumulating sandstone fragments within a soil-like matrix. Added to this, meteoric water permeability strongly differentiates within the weathering zone. Along the southeast-facing bluff of the village, dormant landslides are a common feature. The interface between the bedrock and sliding masses is encountered at the bottom of the weathering zone, forming shallow and elongated landslides. The weathering and the reduction in shear strength during heavy rainfall are considered important factors in triggering these landslides.

## 2.2. Description of Instabilities and Surveying Campaigns

The first known landslide event occurred on 28 January 2021 as a result of heavy rainfall during the previous day (daily total 93.6 mm). A few days later, on 8 February 2021, our team started the systematic mapping and monitoring of the landslide. Fieldwork tasks, such as crack recognition and mapping (Figure 2) and the first UAV flight campaign, were performed over the entire area of interest. The initial landslide extent was measured at a width of 150 m and a length of 250 m (Figure 3). All the flight campaigns were performed with a DJI Phantom 4 Pro UAV and orthophotos were produced using Agisoft Metashape (Figure 3). Cracks were initially recognized, measured, and mapped in the field, and then they were digitized in an ArcMap environment (Figure 3). The extent of the first landslide was measured at 31,906 m<sup>2</sup> (Table 1), while 346 cracks were recorded after the first landslide. As can be easily observed in Figure 3, the dimensions of the cracks vary. Their length ranges from some cm to more than 161 m. In addition, their depth also ranges from 1–2 cm to almost one meter (Figure 3).



**Figure 2.** Fieldwork on 8 February 2021 in Ano Kerassovo village. (**Upper**): A characteristic UAV photo. Cracks are easily detected. The red arrow illustrates one large crack upward from the main road with a depth of almost one meter. (**Bottom**): The same crack as captured from a ground-based perspective.

**Table 1.** Evaluation of the extent of the landslide during the multitemporal surveys.

Date of Field Campaign	Landslide Extent in Square Meters
8 February 2021	31,906
14 December 2021	107,221
25 September 2022	171,747

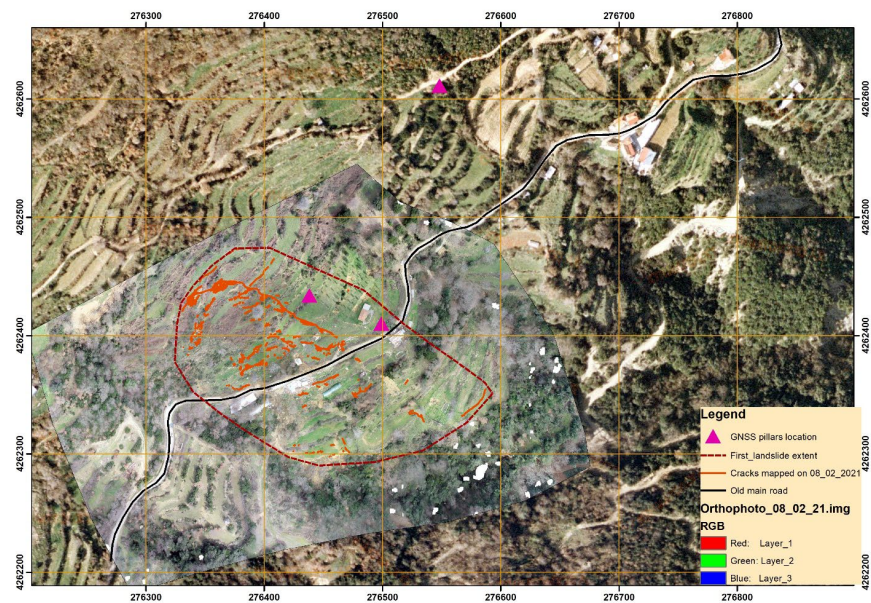


**Figure 3.** Map of the first landslide event as recorded by the UAV campaign on 8 February 2021. The red (dashed) line represents the landslide extent, and the continuous red lines depict the cracks.

The second and more severe event happened on 12 December 2021 as a result of intense rainfall during the previous day (daily total 86 mm). The landslide extent is presented in Figure 4. The landslide extended both in width and length and provoked damage to three of the village houses. The main road of the village was destroyed, and the connection from Ano Kerassovo to Messolonghi was interrupted. As can be noted in Figure 4, the main road (black line) was buried under tons of wasted materials. The width of the landslide reached 380 m, while the length exceeded 380 m. The total extent of the landslide increased by more than 300% in comparison with the initial one, which was estimated at 107,221 m<sup>2</sup>. More than 437 new cracks were detected and digitized from the new orthophoto map (Figure 4). In order to facilitate the reader, the newer cracks are represented in red, and the older ones (from 8 February 2021) are illustrated in blue.

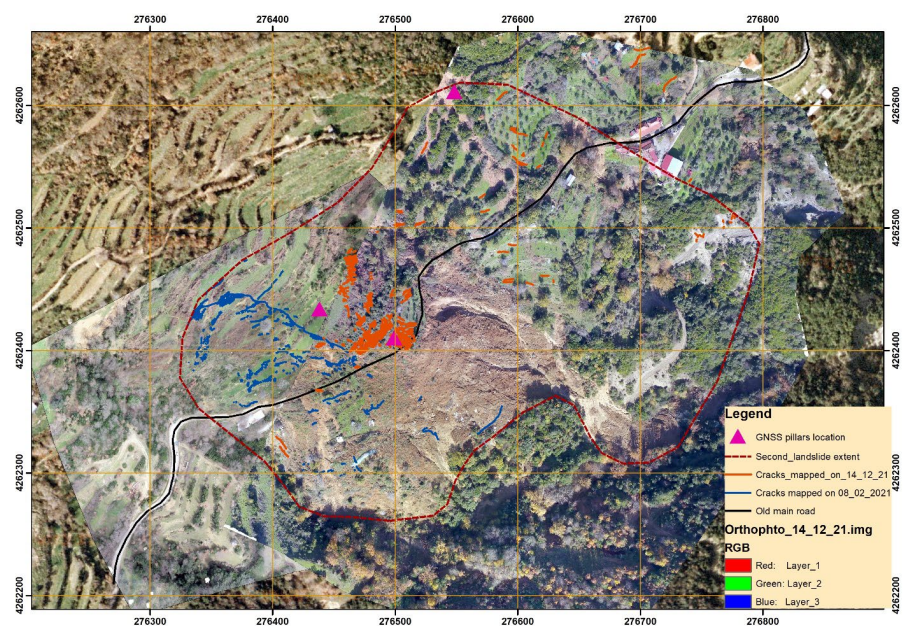


**Figure 4.** Map of the second landslide event as captured on 14 December 2021. The red (dashed) line represents the landslide extent, and the continuous red lines correspond to the cracks. In blue are the cracks that were recorded after the first event on 8 February 2021.

The next field campaign was performed on 25 September 2022 after the summer period and before the beginning of the new hydrological year (1st of October, as specified for Greece). The landslide increased its dimensions in length and width (Table 1 and Figure 5). The width of the landslide reached 480 m, while the length exceeded 520 m. The total extent of the landslide increased by almost 600% in comparison with the initial one, which was estimated at 171,747 m<sup>2</sup>. A total of 524 new cracks were detected and digitized from the new orthophoto map (Figure 5). Their length varied from 0.3 to 36 m. As previously mentioned, the newer cracks are represented in red, and the older ones (from 14 December 2021 and 8 February 2021) are displayed in blue and cyan respectively. It is very important to mention that the new cracks are detected at the edge of the landslide perimeter on the north and west side of the landslide. It is also very important to mention that some new cracks appeared in the northeast part of the orthophoto, about eighty meters east of the previously damaged houses.

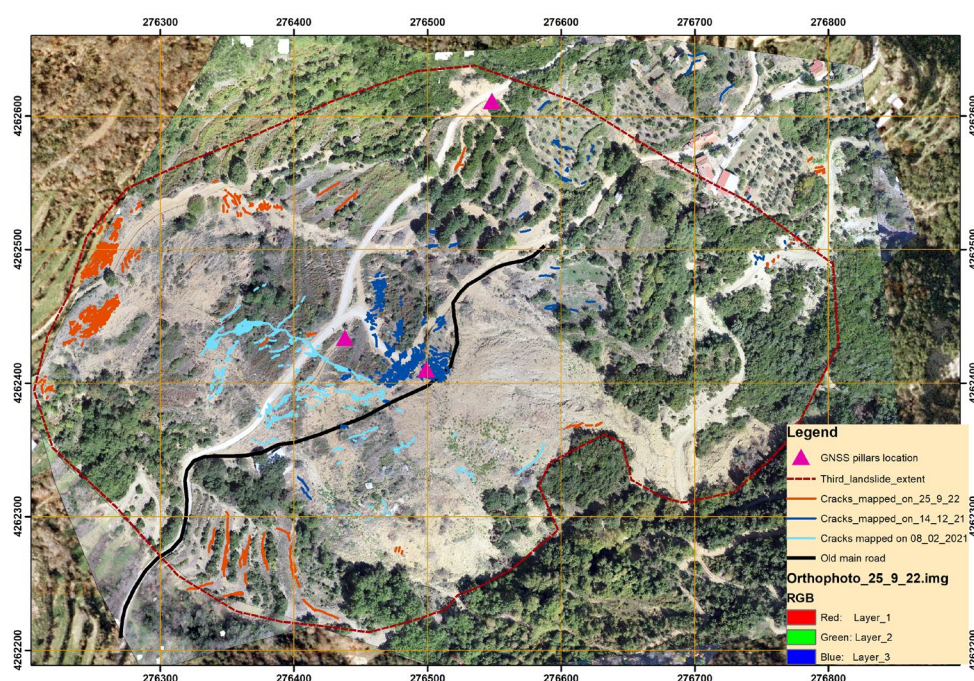


**Figure 5.** Map of the landslide event on 25 September 2022. The red (dashed) line represents the landslide extent, and the continuous red lines display the cracks. In blue and cyan are the cracks that were recorded after the first two events of 2021.

In order to continue the monitoring of the landslide, three permanent pillars for GNSS measurements were installed: two at the center of the landslide and one at the northern edge of the landslide. Those positions are presented with magenta triangles in Figures 2, 4 and 5. The monitoring of the landslide is still ongoing with repeated field campaigns (Table 2).

**Table 2.** Multitemporal monitoring surveys.

Date	Field Measurements	UAV Campaign	GNSS Surveys
8 February 2021	X	X	
14 December 2021	X	X	
25 September 2022	X	X	X
20 December 2022	X	X	X
28 January 2023	X	X	X
11 April 2023	X	X	X

In Figure 6, an overview of the evolution of the landslide extent in the three dates of fieldwork is presented. It can be easily observed that the landslide is growing mainly to the north and east, affecting more and more of the main settlement of Ano Kerassovo.

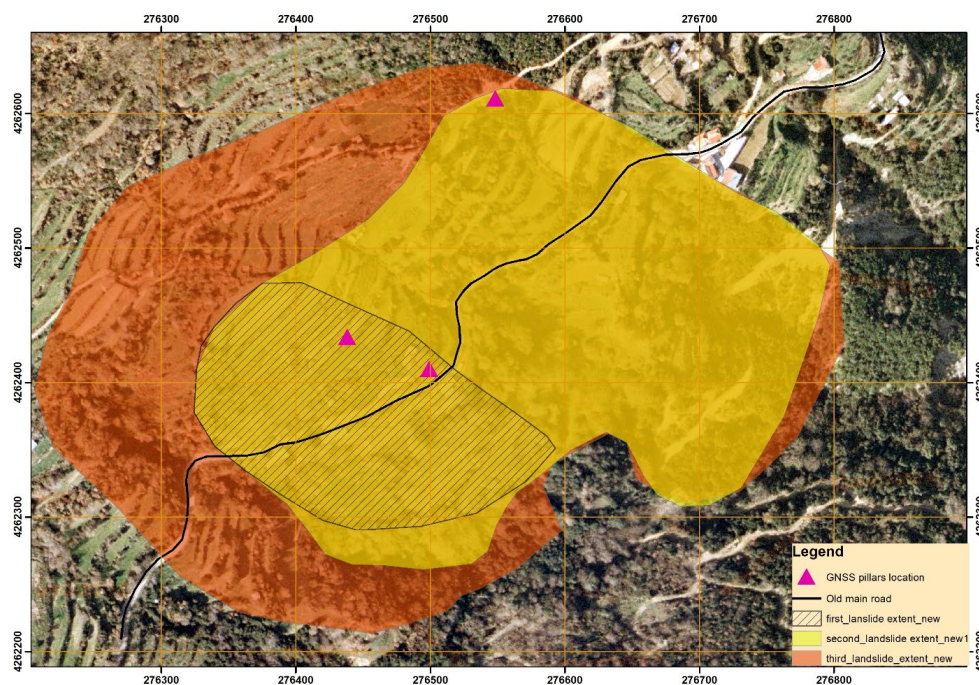


**Figure 6.** An overview of the evolution of the landslide extent. The stripe pattern depicts the landslide extent on 8 February 2021, with yellow representing the landslide area on 14 December 2021 and red representing the extent of the landslide on 25 September 2022.

### 2.3. Meteorological Information

Meteorological data were analyzed in order to examine if there was a correlation between the weather conditions, i.e., precipitation and wind, and landslide occurrence. The nearest permanent meteorological station is situated in Agrinion City. Extended and intense rainfall is the most common triggering mechanism of landslides worldwide, and it is often used for the prediction of slope failures. The statistical graphs, illustrated in Figures 7 and 8, display the annual rainfall statistics as recorded at the nearest local meteorological station, providing a better understanding of the landslide events in the broader area of Ano Kerassovo. Figures 7 and 8 depict the max daily rain in 2021 and 2022 at the Agrinio meteorological station.

As can be noticed from the graphs (Figures 7 and 8), the area experienced heavy rainfall in January 2021, with 93.6 mm of rain, leading to the occurrence of the first landslide event at Ano Kerassovo on 28 January 2021. A data analysis revealed that the index (month/max daily rain 2021) showed a significant decrease from January to July, falling from 93.6 mm to zero. The index then fluctuated over the last five months of the year, with October recording a high point of 88.8 mm and September a low point of 2.4 mm. In detail, four maximum points were noted in January, August, October, and December with 93.6 mm, 87.2 mm, 88.8 mm, and 86.8 mm of rain respectively. This is in accordance with the second and more severe event that manifested on 12 December 2021, proving that apart from rainfall intensity, rainfall duration and a generally wet environment have also a great influence on landslide hazard assessment. As can be observed in the following diagram of rainfall in December 2021, there was 256.8 mm of rain from 3 December to 11 December, and the total rainfall for the whole month was calculated at 299.4 mm (Figure 9).

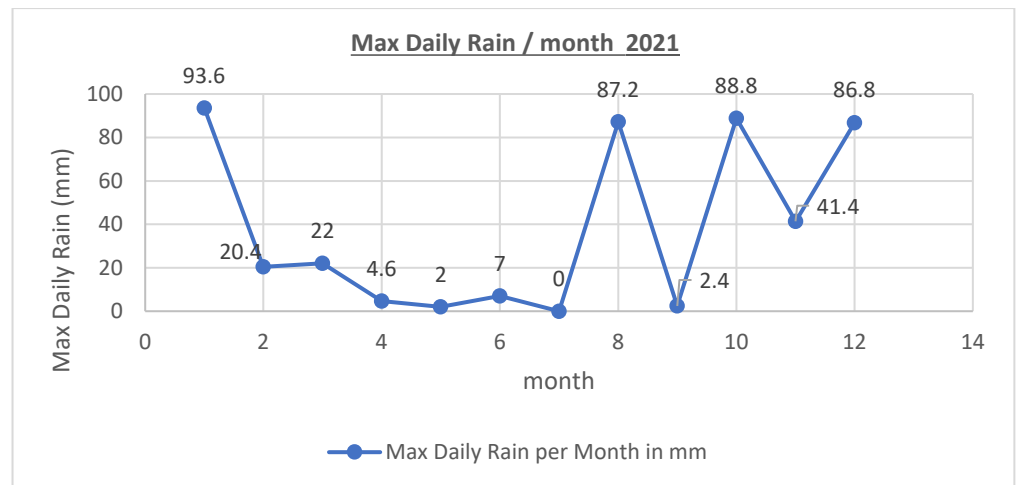


Figure 7. Max daily rainfall per month for 2021 (data obtained from the National Observatory of Athens).

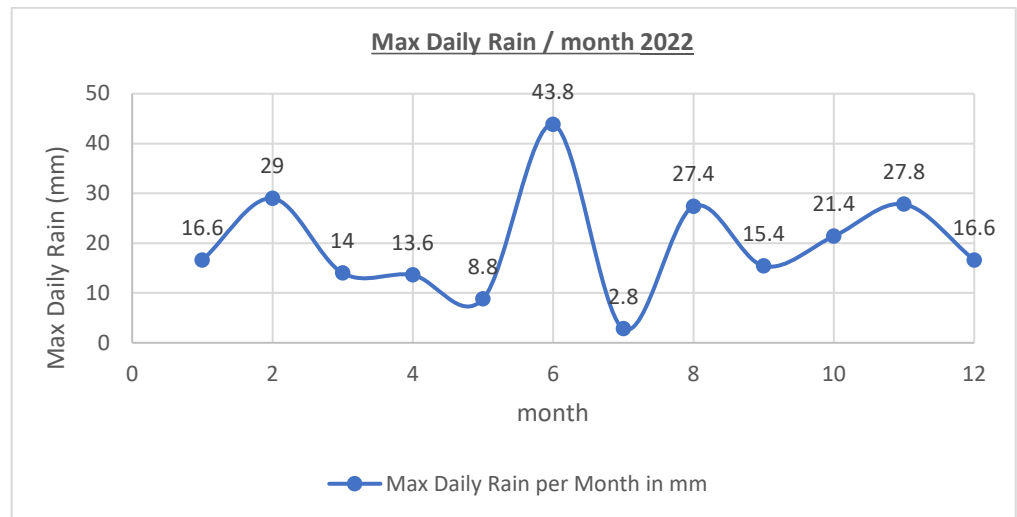


Figure 8. Max daily rainfall per month for 2022 (data obtained from the National Observatory of Athens).

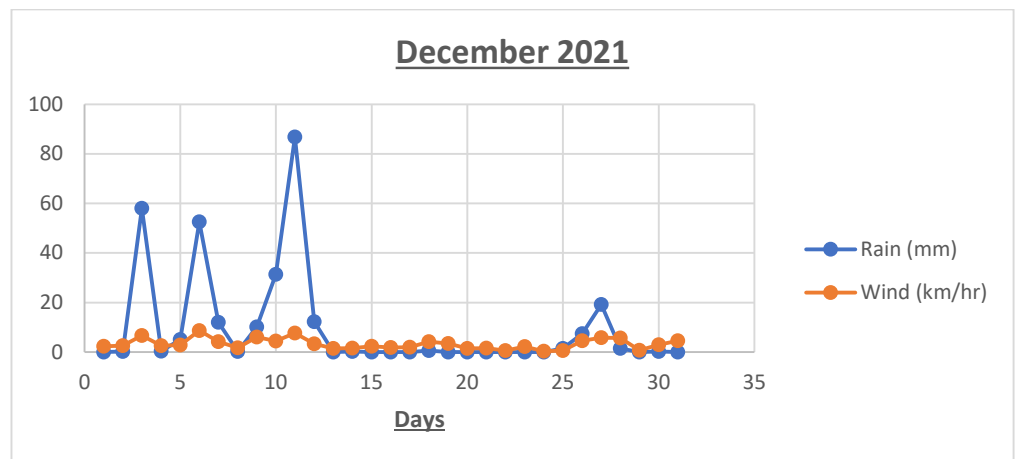


Figure 9. Daily rainfall for December 2021 (data obtained from the National Observatory of Athens).

### 3. Datasets and Methods

The precise mapping and monitoring of the landslide at Ano Kerassovo started a few days after the occurrence of the first slide on 28 January 2021 and continued until today. The last fieldwork took place on 11 April 2023. The surveys were executed at the beginning and the end of the rainy period, as well as on specific dates based on information about the evolution of the area from local residents. Our fieldwork includes the collection of UAV data, as well as high-precision GNSS measurements with 1–2 mm precision (Table 2) in permanent pillars. UAV flights are operated within 1 h using a DJI Phantom 4 Pro. This tetra-copter is easily transferred into the landslide body and can be deployed in a limited space. It is equipped with a 20 MP camera and operates with a mechanical shutter, capturing images of  $5472 \times 3078$  pixels. The flight campaigns were executed at an altitude of 120 m (above ground level), always following the same flight grid. The specific photogrammetric grid retains a 90% along-track and 75% across-track overlap between the acquired photos. Ten square 4.5" black and white targets were allocated sparsely in the field during the UAV surveys. These targets were measured with a real-time kinematic GNSS receiver and used in order to georeference UAV images and enhance the registration quality between the multi-dated orthophotos. All the collected images were processed using the same parameters in Agisoft Metashape software (v. 2.0.1., Agisoft LLC, St. Petersburg, Russia). In order to achieve the best 3D reconstruction, we used the highest-quality option for the alignment of the UAV photos. As described in previous studies [49,50] using the specific option, the camera positions are calculated more accurately. The ultra-high-quality option was also used for dense point cloud generation in order to achieve more detailed and precise depth maps. Regarding other processing steps, such as camera calibration and optimization, the suggested default options were chosen [49,50]. Using the ground control points collected in the field, all the derived products, i.e., orthophotos, and 3D point clouds, were projected to the Hellenic Geodetic Reference System of 1987. The total processing time for the UAV data is estimated at twelve hours.

During the flight campaigns, repetitive static GNSS measurements were performed at three permanent pillars inside the landslide body (Figures 3 and 4). The guideline for the installation of the permanent GNSS pillar positions and the sequent observations were published in [47]. In more detail, these pillars were constructed by excavating a hole and placing a vertical steel rod, which was 1.5 cm thick and 120 cm long. At the top of each pillar, there is a 5/8" pole for the performance of GNSS measurements. Performing static observations on permanent pillars located at key points within the landslide body guarantees the accuracy of the measurements. GNSS measurements were processed using simple mathematical equations in order to calculate the possible deformation from the initial three-axis measurements.

To examine if the archived PSI measurements can be used as future landslide indicators, we obtained data from the European Ground Motion Service (EGMS) [66]. The service provides systematic and accurate (millimeter-scale) ground deformation measurements over the Copernicus-participating countries. Applications such as infrastructure monitoring or geohazard analysis are viable through the service. EGMS measurements are based on the processing of Sentinel-1 imagery using PSI. Buildings, man-made structures, and areas without vegetation are used as permanent scatterers among the multi-temporal Sentinel-1 datasets. The calibration of PSI measurements is performed through data acquired by GNSS. The service distributes three types of products, namely Basic, Calibrated, and Ortho. The Basic level includes ascending and descending line-of-sight velocity maps with annotated geolocalization and quality measures for each point. Calibrated data consist of ascending and descending line-of-sight velocity maps, which are referenced to a model created by GNSS data. Finally, Ortho products provide motion components (horizontal and vertical), which are anchored to a reference geodetic model. In the current research, we utilized Ortho products in the village of Ano Kerassovo.

## 4. Results

### 4.1. UAV Results

To precisely monitor the area of interest, we performed repeated UAV campaigns. The collected data were processed appropriately, and three-dimensional models of the area of interest were generated. Afterward, the generated 3D models were aligned using the iterative closest points (ICPs) algorithm. Figure 10a illustrates the point cloud that emerged from the UAV flight executed on 25 September 2022. The specific point cloud was used as a reference to identify topographic alterations over time. A cloud-to-cloud change detection (C2C) methodology was applied between the reference and the multi-dated point clouds into CloudCompare software. C2C estimates the distance to the closest in the compared cloud for every point. The results of the aforementioned approach are displayed in Figure 10b–d. Specifically, Figure 10b presents the topographic changes between the point clouds, obtained on 25 September 2022 and 20 December 2022. These variations are highlighted in green, and they are related mainly to vegetation changes. Surface deformation occurred between the point clouds, acquired on 25 September 2022 and 25 January 2023, and is depicted with greenish to yellowish shades in Figure 10c. Deformation of the specific period is particularly obvious and intense, with surface changes ranging from 0.7 to 1.8 m. It is evident that rainfall events strongly affected the entire region. The most recent UAV campaign, performed on 11 April 2023, revealed that the landslide is still active, but the prevailing force is the at-depth erosion, which shapes the study area relief. This is clearly noticeable in Figure 10d, in which more areas have been altered.

### 4.2. GNSS Results

The installed permanent GNSS pillars were also surveyed during the repeated field campaigns (Table 2). The northern observation position was covered by landslide material a few months after installation. Therefore, GNSS analysis was performed only on the remaining two positions. The analysis of the GNSS time series is depicted in Figure 11a,b. The charts display the variations of the three-axis coordinates in time. As can be observed, permanent pillar 1 presents the greatest topographic changes, reaching 7 cm of deformation on the  $x$ -axis and almost 25 cm on the  $y$ -axis within the last four months. The vertical deformation was measured at 7 cm for the same period. Concerning permanent pillar 2, surface variations are measured at 10 cm for the  $x$ -axis and 20 cm for the  $y$ -axis. Overall, the larger deformation is detected in the  $y$ -axis, which is aligned to the landslide azimuth direction.

### 4.3. PSI Analysis

To extend the observation period and fully understand landslide evolution and dynamics, we acquired PSI measurements from the EGMS. PSI locations are displayed in red dots in Figure 12. As can be noticed, there is a PSI location within the current extent of the landslide. The specific point presents a surface deformation between 2016 and 2021, estimated at 4.10 mm/year. The more detailed analysis of the time series demonstrated that archived PSI captured the initial landslide deformation phenomena. In particular, a sudden 2 cm subsidence was observed in the time series after the occurrence of the first landslide episode on 28 January 2021. This subsidence is marked with a dashed black rectangular in Figure 13. In light of this, we examined PSI deformation rates over the entire village. We noticed that there were other two gradually deforming points inside the settlement, displaying almost identical subsidence rates (Figure 12).

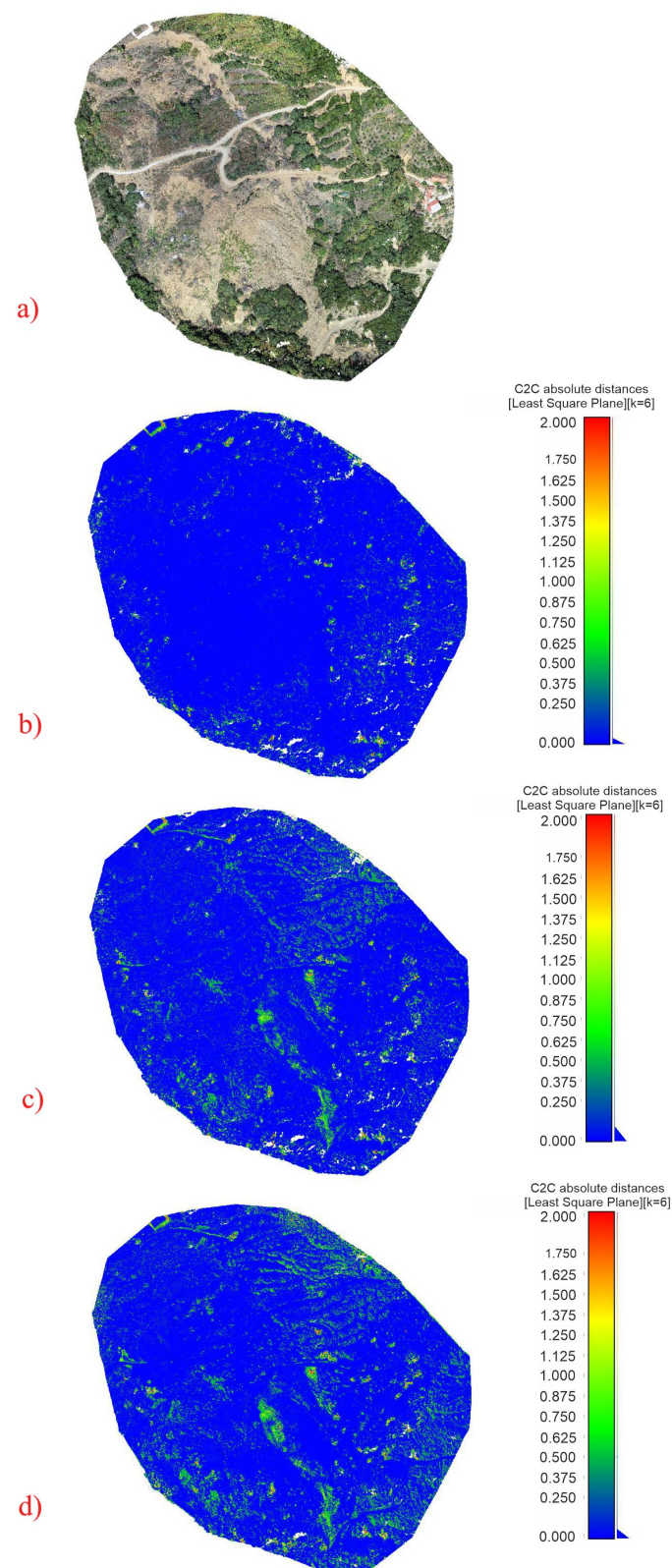


**Figure 10.** Cloud-to-cloud comparison. (a) Initial UAV point cloud acquired on 25 September 2022. (b) C2C distances calculated between the point cloud of 25 September 2022 and the respective point cloud of 20 December 2022. (c) C2C distances calculated between the point cloud of 25 September 2022 and the respective point cloud of 28 January 2023. (d) C2C distances calculated between the point cloud of 25 September 2022 and the respective point cloud of 11 April 2023.

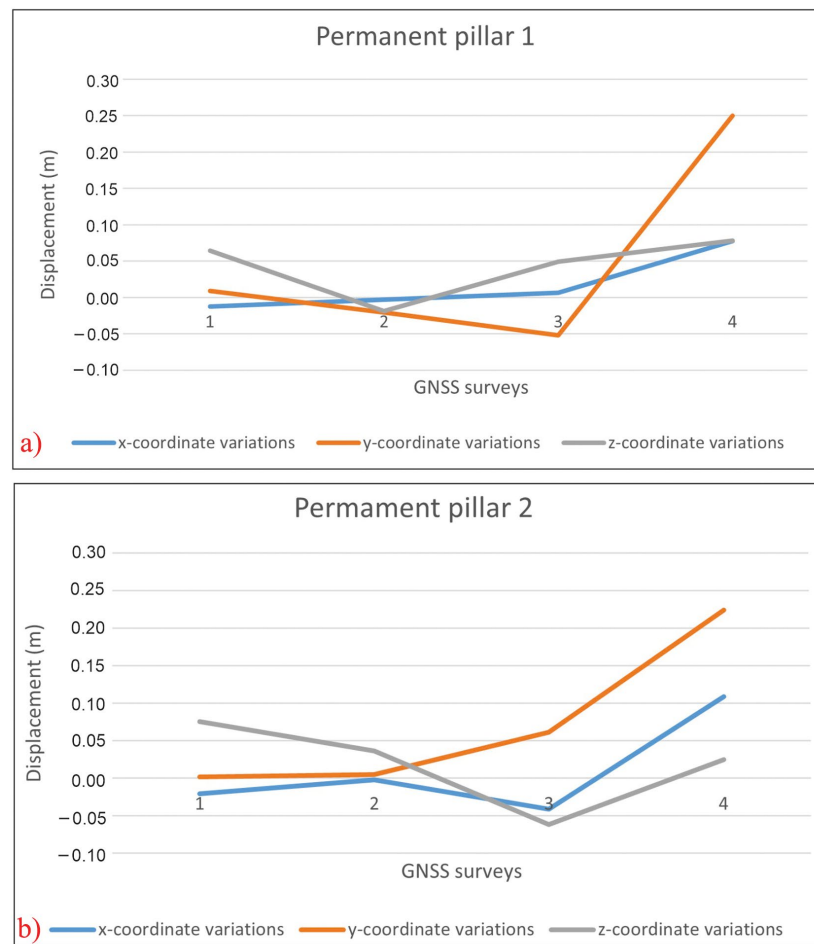


**Figure 11.** (a) GNSS variations of the coordinates of permanent pillar 1 over time. The x-axis corresponds to the multitemporal GNSS surveys, while the y-axis illustrates the calculated displacements. (b) GNSS variations of the coordinates of permanent pillar 2 over time. The x-axis corresponds to the multitemporal GNSS surveys, while the y-axis illustrates the calculated displacements.

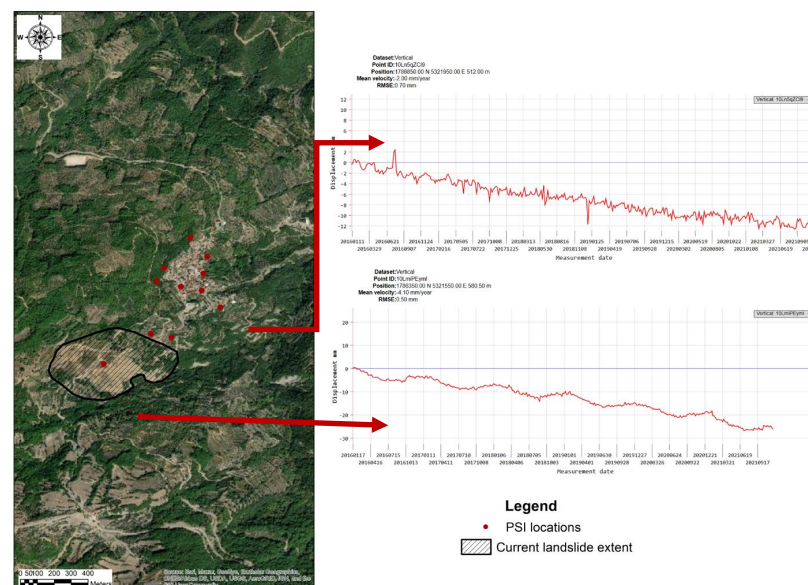


**Figure 12.** Analysis of the archived PSI measurements.

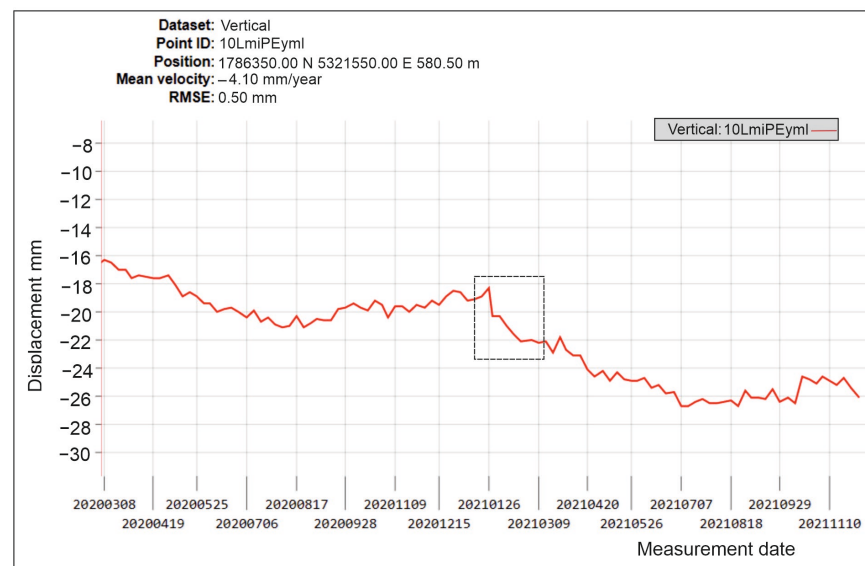


**Figure 13.** PSI measurements in the landslide area. After the occurrence of the first landslide episode on 28 January 2021, subsidence is marked with a dashed black rectangular box.

## 5. Discussion

In the current study, UAV-derived products, GNSS measurements, and field observations were combined with archived PSI data in order to monitor and predict the possible evolution of an active landslide in Ano Kerassovo village. The results from the UAV point clouds comparison, the measurements of the permanent GNSS pillars, and the field observations lead to the conclusion that the landslide is always active and right now is in the vertical erosion phase. As can easily be noticed in Figure 14, there are many deep cracks on the main road and in the whole landslide body. Those cracks are the beginning of new deformations and mass wasting that explain the volume differences that are measured in the point clouds comparison.



**Figure 14.** Field observations. (a) Spatial distribution of the crack across the road (b). In-depth erosion along the crack.

It was proven that the main triggering factor for the landslide occurrence was heavy rainfall. The first landslide event was manifested after a daily rainfall height of 93.6 mm, while a total rainfall of 256.8 mm within a week triggered the second reactivation. Since then, the landslide is still active, presenting slower deformation rates, as rainfall height was lower during 2022 than in previous years.

There are many studies published in the last years pointing out the usefulness of InSAR techniques, UAV photogrammetry, and GNSS technology for landslide monitoring. However, there are very few combining all the previously mentioned techniques.

Our methodology and results are in accordance with some previously published studies. Eker and Aydin 2021 also used archived PSI data, aerial photos, and UAV images in order to monitor an active landslide long-term [57]. They also used a 3D point cloud comparison in order to measure the volume deformation. In another similar study by Razi [59], PSI analysis was performed on ALOS PALSAR data, and the results were compared to UAV data and GNSS measurements. Other researchers combined GNSS measurements, UAV data, ground-penetrating radar data, and geotechnical techniques in order to monitor a landslide in Romania. Using interdisciplinary monitoring, it was proven that the slope was undergoing surface erosion, and soil displacements were detected [60]. A combination of PSI data and UAV photogrammetry was also presented by [56]. In particular, they used PSI data derived from 25 ENVISAT SAR images and UAV photogrammetry to monitor displacements in a resort in Granada, Spain. Themistocleous et al. presented an integrated ground deformation monitoring study by combining INSAR data, UAV imagery, and GNSS measurements [58]. The study area was a UNESCO World Heritage Site in Cyprus named Choirokoitia.

A noticeable novelty in the current study is the effort to predict the future evolution of the specific landslide based on archived PSI data and the UAV and GNSS measurements. Figure 15 presents an overview of the broader area. The landslide extents at different dates and the position of the PSI are displayed together.

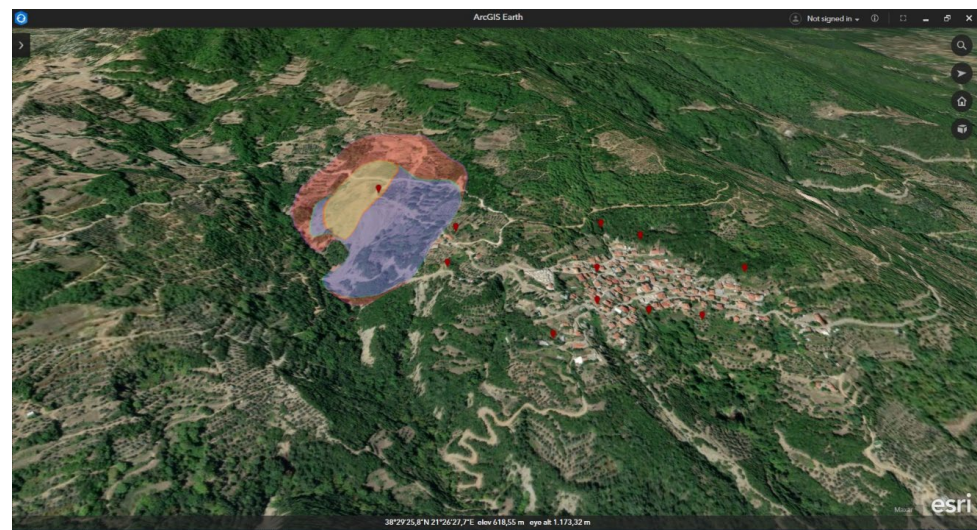


**Figure 15.** Overall view of the multitemporal landslide extents along with PSI locations. The different colors display the evolution of the landslide over time, while the red dots correspond to PSI locations.

Inside the landslide body, there was a PSI measurement that is allocated almost in the center of the sliding area. It is included in the first landslide perimeter. The specific PSI measurement demonstrated a pure subsidence of  $-4.1$  mm/y for the five-year period from 2016 to 2021. This subsidence could be a warning signal for the landslide occurrence. Inside Ano Kerassovo village, there are two PSI measurements depicting subsidence estimated at 2 mm/y. These points should be regularly monitored for future landslide events. In addition to GNSS measurements and crack mapping from the UAV orthophotos, we

assume that the landslide will progress to the northeast in the near future. The time of the expansion depends on the rainfall, which remains the main triggering factor.

## 6. Conclusions

A large landslide affecting Ano Kerassovo village in Western Greece is monitored using UAV images, GNSS measurements, and archived PSI data obtained from the European Ground Motion Service. The key points of the current study are summarized below:

- The occurrence of the landslide in January 2021 and its reactivation in December 2021 were both triggered by heavy rainfall.
- The landslide is still active and, in the current period, is in the vertical erosion phase.
- PSI measurements from 2015 to 2021 demonstrated high subsidence rates at many points inside and outside the landslide body.
- It is proven that archived PSI measurements can be used as an indicator of possible landslide initialization points.
- PSI measurements can be used for small-scale large area investigations, while UAV and GNSS data can precisely identify microscale deformations.

Considering all aspects, we assume that the landslide will be expanded in a northeastern direction.

Summarizing the current study, it is proven that multidisciplinary remote sensing methodologies can provide the necessary information to study landslide evolution in different scales and extents. The same approach can be applied in other monitoring applications such as volcanic monitoring, mine monitoring, and monitoring of subsidence related to human activities. However, some limitations of the technique should be taken into account, such as (a) the proper execution of UAV and GNSS campaigns and (b) the correct interpretation of the results.

**Author Contributions:** Conceptualization, K.G.N., A.K. and I.K.K.; methodology, K.G.N. and A.K.; software, K.G.N., A.K. and N.T.; investigation, K.G.N., A.K., E.L. and I.K.K.; writing—original draft preparation, K.G.N., A.K., E.L. and I.K.K.; writing—review and editing, K.G.N. and A.K.; supervision, K.G.N. and I.K.K.; project administration, K.G.N. All authors have read and agreed to the published version of the manuscript.

**Funding:** This research received no external funding.

**Data Availability Statement:** Data are available upon request due to restrictions. The data presented in this study are available upon request from the corresponding author. The data are not publicly available due to public safety reasons.

**Acknowledgments:** The authors are thankful to the European Ground Motion Service (EGMS) and Copernicus program for the free distribution of PSI measurements.

**Conflicts of Interest:** The authors declare no conflict of interest.

## References

1. Petley, D. Global patterns of loss of life from landslides. *Geology* **2012**, *40*, 927–930. [[CrossRef](#)]
2. Vranken, L.; Van Turnhout, P.; Van Den Eeckhaut, M.; Vandekerckhove, L.; Poesen, J. Economic valuation of landslide damage in hilly regions: A case study from Flanders, Belgium. *Sci. Total Environ.* **2013**, *447*, 323–336. [[CrossRef](#)]
3. Vranken, L.; Vantilt, G.; Van Den Eeckhaut, M.; Vandekerckhove, L.; Poesen, J. Landslide risk assessment in a densely populated hilly area. *Landslides* **2015**, *12*, 787–798. [[CrossRef](#)]
4. Conforti, M.; Ietto, F. An integrated approach to investigate slope instability affecting infrastructures. *Bull. Eng. Geol. Environ.* **2019**, *78*, 2355–2375. [[CrossRef](#)]
5. Wu, X.; Chen, X.; Zhan, F.B.; Hong, S. Global research trends in landslides during 1991–2014: A bibliometric analysis. *Landslides* **2015**, *12*, 1215–1226. [[CrossRef](#)]
6. Galve, J.P.; Cevasco, A.; Brandolini, P.; Piacentini, D.; Azañón, J.M.; Notti, D.; Soldati, M. Cost-based analysis of mitigation measures for shallow-landslide risk reduction strategies. *Eng. Geol.* **2016**, *213*, 142–157. [[CrossRef](#)]
7. Carrión-Mero, P.; Montalván-Burbano, N.; Morante-Carballo, F.; Quesada-Román, A.; Apolo-Masache, B. Worldwide research trends in landslide science. *Int. J. Environ. Res. Public Health* **2021**, *18*, 9445. [[CrossRef](#)] [[PubMed](#)]

8. Senouci, R.; Taibi, N.-E.; Teodoro, A.C.; Duarte, L.; Mansour, H.; Yahia Meddah, R. GIS-Based Expert Knowledge for Landslide Susceptibility Mapping (LSM): Case of Mostaganem Coast District, West of Algeria. *Sustainability* **2021**, *13*, 630. [[CrossRef](#)]
9. Conforti, M.; Ietto, F. Influence of Tectonics and Morphometric Features on the Landslide Distribution: A Case Study from the Mesima Basin (Calabria, South Italy). *J. Earth Sci.* **2020**, *31*, 393–409. [[CrossRef](#)]
10. Quesada-Román, A.; Fallas-López, B.; Hernández-Espinoza, K.; Stoffel, M.; Ballesteros-Cánovas, J.A. Relationships between earthquakes, hurricanes, and landslides in Costa Rica. *Landslides* **2019**, *16*, 1539–1550. [[CrossRef](#)]
11. Raspini, F.; Bianchini, S.; Ciampalini, A.; Del Soldato, M.; Montalti, R.; Solari, L.; Tofani, V.; Casagli, N. Persistent Scatterers continuous streaming for landslide monitoring and mapping: The case of the Tuscany region (Italy). *Landslides* **2019**, *16*, 2033–2044. [[CrossRef](#)]
12. Casagli, N.; Cigna, F.; Bianchini, S.; Hölbling, D.; Füreder, P.; Righini, G.; del Conte, S.; Friedl, B.; Schneiderbauer, S.; Iasio, C.; et al. Landslide mapping and monitoring by using radar and optical remote sensing: Examples from the EC-FP7 project SAFER. *Remote Sens. Appl. Soc. Environ.* **2016**, *4*, 92–108. [[CrossRef](#)]
13. Massonnet, D.; Feigl, K.L. Radar interferometry and its application to changes in the Earth's surface. *Rev. Geophys.* **1998**, *36*, 441–500. [[CrossRef](#)]
14. Herrera, G.; Notti, D.; García-Davalillo, J.C.; Mora, O.; Cooksley, G.; Sánchez, M.; Crosetto, M. Analysis with C-and X-band satellite SAR data of the Portalet landslide area. *Landslides* **2011**, *8*, 195–206. [[CrossRef](#)]
15. Zhao, C.; Kang, Y.; Zhang, Q.; Lu, Z.; Li, B. Landslide identification and monitoring along the Jinsha River catchment (Wudongde reservoir area), China, using the InSAR method. *Remote Sens.* **2018**, *10*, 993. [[CrossRef](#)]
16. Wasowski, J.; Bovenga, F. Investigating landslides and unstable slopes with satellite Multi Temporal Interferometry: Current issues and future perspectives. *Eng. Geol.* **2014**, *174*, 103–138. [[CrossRef](#)]
17. Schlögel, R.; Doubre, C.; Malet, J.P.; Masson, F. Landslide deformation monitoring with ALOS/PALSAR imagery: A D-InSAR geomorphological interpretation method. *Geomorphology* **2015**, *231*, 314–330. [[CrossRef](#)]
18. Ferretti, A.; Prati, C.; Rocca, F. Permanent Scatterers in SAR interferometry. *IEEE Trans. Geosci. Remote Sens.* **2001**, *39*, 8–20. [[CrossRef](#)]
19. Crosetto, M.; Monserrat, O.; Cuevas-González, M.; Devanthery, N.; Crippa, B. Persistent Scatterer Interferometry: A Review. *ISPRS J. Photogramm. Remote Sens.* **2016**, *115*, 78–89. [[CrossRef](#)]
20. Tofani, V.; Raspini, F.; Catani, F.; Casagli, N. Persistent Scatterer Interferometry (PSI) technique for landslide characterization and monitoring. *Remote Sens.* **2013**, *5*, 1045–1065. [[CrossRef](#)]
21. Lanari, R.; Mora, O.; Manunta, M.; Mallorquí, J.J.; Berardino, P.; Sansosti, E. A small baseline approach for investigating deformation on full resolution differential SAR interferograms. *IEEE Trans. Geosci. Remote Sens.* **2004**, *42*, 1377–1386. [[CrossRef](#)]
22. Berardino, P.; Fornaro, G.; Lanari, R.; Sansosti, E. A new algorithm for surface deformation monitoring based on small baseline differential SAR interferograms. *IEEE Trans. Geosci. Remote Sens.* **2003**, *40*, 2375–2383. [[CrossRef](#)]
23. Pasquali, P.; Cantone, A.; Riccardi, P.; Defilippi, M.; Ogushi, F.; Gagliano, S.; Tamura, M. Mapping of Ground Deformations with Interferometric Stacking Techniques. In *Land Applications of Radar Remote Sensing*; InTech: London, UK, 2014. [[CrossRef](#)]
24. Crippa, C.; Agliardi, F. Practical Estimation of Landslide Kinematics Using PSI Data. *Geosciences* **2021**, *11*, 214. [[CrossRef](#)]
25. Cigna, F.; Bianchini, S.; Casagli, N. How to assess landslide activity and intensity with Persistent Scatterer Interferometry (PSI): The PSI-based matrix approach. *Landslides* **2013**, *10*, 267–283. [[CrossRef](#)]
26. Nefros, C.; Alataz, S.; Loupasakis, C.; Kontoes, C. Persistent Scatterer Interferometry (PSI) Technique for the Identification and Monitoring of Critical Landslide Areas in a Regional and Mountainous Road Network. *Remote Sens.* **2023**, *15*, 1550. [[CrossRef](#)]
27. Aslan, G.; Fomelis, M.; Raucoules, D.; de Michele, M.; Bernardie, S.; Cakir, Z. Landslide mapping and monitoring using persistent scatterer interferometry (PSI) technique in the French alps. *Remote Sens.* **2020**, *12*, 1305. [[CrossRef](#)]
28. Gili, J.A.; Corominas, J.; Rius, J. Using Global Positioning System Techniques in Landslide Monitoring. *Eng. Geol.* **2000**, *55*, 167–192. [[CrossRef](#)]
29. Huang, G.; Du, S.; Wang, D. GNSS techniques for real-time monitoring of landslides: A review. *Satell. Navig.* **2023**, *4*, 5. [[CrossRef](#)]
30. Wang, P.; Liu, H.; Nie, G.; Yang, Z.; Wu, J.; Qian, C.; Shu, B. Performance evaluation of a real-time high-precision landslide displacement detection algorithm based on GNSS virtual reference station technology. *Meas. J. Int. Meas. Confed.* **2022**, *199*, 111457. [[CrossRef](#)]
31. Huang, G.; Wang, D.; Du, Y.; Zhang, Q.; Bai, Z.; Wang, C. Deformation Feature Extraction for GNSS Landslide Monitoring Series Based on Robust Adaptive Sliding-Window Algorithm. *Front. Earth Sci.* **2022**, *10*, 487. [[CrossRef](#)]
32. Šegina, E.; Peternel, T.; Urbančič, T.; Realini, E.; Zupan, M.; Jež, J.; Caldera, S.; Gatti, A.; Tagliaferro, G.; Consoli, A.; et al. Monitoring surface displacement of a deep-seated landslide by a low-cost and near real-time GNSS system. *Remote Sens.* **2020**, *12*, 3375. [[CrossRef](#)]
33. Cina, A.; Piras, M. Performance of low-cost GNSS receiver for landslides monitoring: Test and results. *Geomatics. Nat. Hazards Risk* **2015**, *6*, 497–514. [[CrossRef](#)]
34. Lucieer, A.; Jong, S.M.D.; Turner, D. Mapping landslide displacements using Structure from Motion (SfM) and image correlation of multi-temporal UAV photography. *Prog. Phys. Geogr.* **2014**, *38*, 97–116. [[CrossRef](#)]
35. Catani, F. Landslide detection by deep learning of non-nadir and crowdsourced optical images. *Landslides* **2020**, *18*, 1025–1044. [[CrossRef](#)]

36. Rau, J.; Jhan, J.; Lo, C.; Lin, Y. Landslide mapping using imagery acquired by a fixed-wing UAV. *Int. Arch. Photogramm. Remote Sens. Spat. Inf. Sci.* **2011**, *38*, 195–200. [[CrossRef](#)]
37. Shi, B.; Liu, C. UAV for landslide mapping and deformation analysis. In Proceedings of the International Conference on Intelligent Earth Observing and Applications, International Society for Optics and Photonics, Guilin, China, 23–24 October 2015; Volume 9808. [[CrossRef](#)]
38. Peternel, T.; Kumelj, Š.; Oštir, K.; Komac, M. Monitoring the Potoška planina landslide (NW Slovenia) using UAV photogrammetry and tachymetric measurements. *Landslides* **2017**, *14*, 395–406. [[CrossRef](#)]
39. Cignetti, M.; Godone, D.; Wrzesniak, A.; Giordan, D. Structure from motion multisource application for landslide characterization and monitoring: The champlas du col case study, sestriere, North-Western Italy. *Sensors* **2019**, *19*, 2364. [[CrossRef](#)] [[PubMed](#)]
40. Antoine, R.; Lopez, T.; Tanguy, M.; Lissak, C.; Gailler, L.; Labazuy, P.; Fauchard, C. Geoscientists in the sky: Unmanned aerial vehicles responding to geohazards. *Surv. Geophys* **2020**, *41*, 1285–1321. [[CrossRef](#)]
41. Kyriou, A.; Nikolakopoulos, K.G.; Koukouvelas, I.K. Timely and Low-Cost Remote Sensing Practices for the Assessment of Landslide Activity in the Service of Hazard Management. *Remote Sens.* **2022**, *14*, 4745. [[CrossRef](#)]
42. Chen, Z.; Zhou, H.; Ye, F.; Liu, B.; Fu, W. The characteristics, induced factors, and formation mechanism of the 2018 Baige landslide in Jinsha River, Southwest China. *Catena* **2021**, *203*, 105337. [[CrossRef](#)]
43. Yang, D.; Qiu, H.; Hu, S.; Pei, Y.; Wang, X.; Du, C.; Long, Y.; Cao, M. Influence of successive landslides on topographic changes revealed by multitemporal high-resolution UAS-based DEM. *Catena* **2021**, *202*, 105229. [[CrossRef](#)]
44. Teodoro, A.; Santos, P.; Espinha Marques, J.; Ribeiro, J.; Mansilha, C.; Melo, A.; Duarte, L.; Rodrigues de Almeida, C.; Flores, D. An Integrated Multi-Approach to Environmental Monitoring of a Self-Burning Coal Waste Pile: The São Pedro da Cova Mine (Porto, Portugal) Study Case. *Environments* **2021**, *8*, 48. [[CrossRef](#)]
45. Rossi, G.; Tanteri, L.; Tofani, V.; Vannocci, P.; Moretti, S.; Casagli, N. Multitemporal UAV surveys for landslide mapping and characterization. *Landslides* **2018**, *15*, 1045–1052. [[CrossRef](#)]
46. Ilinca, V.; Şandric, I.; Chiţu, Z.; Irimia, R.; Gheuca, I. UAV applications to assess short-term dynamics of slow-moving landslides under dense forest cover. *Landslides* **2022**, *19*, 1717–1734. [[CrossRef](#)]
47. Kyriou, A.; Nikolakopoulos, K.; Koukouvelas, I.; Lampropoulou, P. Repeated UAV Campaigns, GNSS Measurements, GIS, and Petrographic Analyses for Landslide Mapping and Monitoring. *Minerals* **2021**, *11*, 300. [[CrossRef](#)]
48. Al-Rawabdeh, A.; Moussa, A.; Foroutan, M.; El-Sheimy, N.; Habib, A. Time series UAV image-based point clouds for landslide progression evaluation applications. *Sensors* **2017**, *17*, 2378. [[CrossRef](#)]
49. Nikolakopoulos, K.G.; Kyriou, A.; Koukouvelas, I.K. Developing a Guideline of Unmanned Aerial Vehicle's Acquisition Geometry for Landslide Mapping and Monitoring. *Appl. Sci.* **2022**, *12*, 4598. [[CrossRef](#)]
50. Kyriou, A.; Nikolakopoulos, K.; Koukouvelas, I. How Image Acquisition Geometry of UAV Campaigns Affects the Derived Products and Their Accuracy in Areas with Complex Geomorphology. *ISPRS Int. J. Geo-Inf.* **2021**, *10*, 408. [[CrossRef](#)]
51. Rodriguez-Caballero, E.; Rodriguez-Lozano, B.; Segura-Tejada, R.; Blanco-Sacristán, J.; Cantón, Y. Landslides on dry badlands: UAV images to identify the drivers controlling their unexpected occurrence on vegetated hillslopes. *J. Arid. Environ.* **2021**, *187*, 104434. [[CrossRef](#)]
52. Hastaoğlu, K.Ö.; Gül, Y.; Poyraz, F.; Kara, B.C. Monitoring 3D areal displacements by a new methodology and software using UAV photogrammetry. *Int. J. Appl. Earth Obs. Geoinf.* **2019**, *83*, 101916. [[CrossRef](#)]
53. Teo, T.A.; Fu, Y.J.; Li, K.W.; Weng, M.C.; Yang, C.M. Comparison between image- and surface-derived displacement fields for landslide monitoring using an unmanned aerial vehicle. *Int. J. Appl. Earth Obs. Geoinf* **2023**, *116*, 103164. [[CrossRef](#)]
54. Comert, R.; Avdan, U.; Gorum, T.; Nefeslioglu, H.A. Mapping of shallow landslides with object-based image analysis from unmanned aerial vehicle data. *Eng. Geol.* **2019**, *260*, 105264. [[CrossRef](#)]
55. Cheng, Z.; Gong, W.; Tang, H.; Juang, C.H.; Deng, Q.; Chen, J.; Ye, X. UAV photogrammetry-based remote sensing and preliminary assessment of the behavior of a landslide in Guizhou, China. *Eng. Geol.* **2021**, *289*, 106172. [[CrossRef](#)]
56. Mateos, R.M.; Azañón, J.M.; Roldán, F.J.; Notti, D.; Pérez-Peña, V.; Galve, J.P.; Pérez-García, J.L.; Colomo, C.M.; Gómez-López, J.M.; Montserrat, O.; et al. The combined use of PSInSAR and UAV photogrammetry techniques for the analysis of the kinematics of a coastal landslide affecting an urban area (SE Spain). *Landslides* **2017**, *14*, 743–754. [[CrossRef](#)]
57. Eker, R.; Aydın, A. Long-term retrospective investigation of a large, deep-seated, and slow-moving landslide using InSAR time series, historical aerial photographs, and UAV data: The case of Devrek landslide (NW Turkey). *Catena* **2021**, *196*, 104895. [[CrossRef](#)]
58. Themistocleous, K.; Danezis, C.; Gikas, V. Monitoring ground deformation of cultural heritage sites using SAR and geodetic techniques: The case study of Choirokoitia, Cyprus. *Appl. Geomat.* **2021**, *13*, 37–49. [[CrossRef](#)]
59. Razi, P.; Sumantyo, J.T.S.; Perissin, D.; Kuze, H.; Chua, M.Y.; Panggabean, G.F. 3D land mapping and land deformation monitoring using persistent scatterer interferometry (PSI) ALOS PALSAR: Validated by Geodetic GPS and UAV. *IEEE Access* **2018**, *6*, 12395–12404. [[CrossRef](#)]
60. Sestras, P.; Bilaşco, Ş.; Roşca, S.; Veres, I.; Ilies, N.; Hysa, A.; Spalević, V.; Cîmpeanu, S.M. Multi-Instrumental Approach to Slope Failure Monitoring in a Landslide Susceptible Newly Built-Up Area: Topo-Geodetic Survey, UAV 3D Modelling and Ground-Penetrating Radar. *Remote Sens.* **2022**, *14*, 5822. [[CrossRef](#)]
61. Underhill, J. Late Cenozoic deformation of the Hellenide foreland, Western Greece. *Geol. Soc. Am. Bull.* **1989**, *101*, 613–634. [[CrossRef](#)]

62. Skourlis, K.; Doutsos, T. The Pindos Fold-and-thrust belt (Greece): Inversion kinematics of a passive continental margin. *Int. J. Earth Sci.* **2013**, *92*, 891–903. [[CrossRef](#)]
63. Sotiropoulos, S.; Kamberis, E.; Triantaphyllou, M.V.; Doutsos, T. Thrust sequences in the central part of the External Hellenides. *Geol. Mag.* **2003**, *140*, 661–668. [[CrossRef](#)]
64. Xypolias, P.; Koukouvelas, I.K. Paleostress magnitude in a Fold-Thrust Belt (External Hellenides, Greece): Evidence from twinning in calcareous rocks. *Episodes* **2005**, *28*, 245–251. [[CrossRef](#)]
65. Sotiropoulos, S.; Triantaphyllou, M.V.; Kamberis, E.; Tsaila-Monopolis, S. Paleogene terrigenous (flysch) sequences in Etoloakarnania region (W. Greece). Plankton stratigraphy and paleoenvironmental implications. *Geobios* **2008**, *41*, 415–433. [[CrossRef](#)]
66. EGMS. Available online: <https://land.copernicus.eu/pan-european/european-ground-motion-service> (accessed on 10 April 2023).

**Disclaimer/Publisher’s Note:** The statements, opinions and data contained in all publications are solely those of the individual author(s) and contributor(s) and not of MDPI and/or the editor(s). MDPI and/or the editor(s) disclaim responsibility for any injury to people or property resulting from any ideas, methods, instructions or products referred to in the content.